

# In Situ Printing: Insights into the Morphology Formation and Optical Property Evolution of Slot-Die-Coated Active Layers Containing Low Bandgap Polymer Donor and Nonfullerene Small Molecule Acceptor

Kerstin S. Wienhold, Volker Körstgens, Sebastian Grott, Xinyu Jiang, Matthias Schwartzkopf, Stephan V. Roth, and Peter Müller-Buschbaum\*

Printing of active layers for high-efficiency organic solar cells with the slot-die coating technique can overcome the challenge of upscaling, which will be needed for organic photovoltaics on its way to marketability. The morphology of a bulk-heterojunction organic solar cell has a very high impact on its power conversion efficiency. Therefore, it is of particular importance to understand the mechanisms of structure formation during printing of active layers to enable further optimization of the solar cell performance and upscaling of the production process. Meniscus-guided slot-die coating of the blend of a low bandgap conjugated polymer donor with benzodithiophene units PBDB-T-SF and the nonfullerene small molecule acceptor IT-4F is studied in situ with optical microscopy, Ultraviolet–visible spectroscopy, and grazing incidence small angle X-ray scattering. The structure formation is followed from the liquid to the final dry film state. Thereby, five regimes of morphology formation are determined. The morphological evolution in the printed active layer is correlated to changing optical properties of the thin film. In the final dry film, polymer domains of several tens of nanometers are observed, which will be favorable for application in high-efficiency organic solar cells.

Examples are solar trees, solar windows, and functional clothes.<sup>[1–5]</sup> Recent research mainly focused on the identification and synthesis of new high-efficiency polymer donors and small molecule acceptors with outstanding solar cell performance.<sup>[6–11]</sup> In particular, the use of nonfullerene small molecule acceptors marked the next breakthrough in device efficiencies after the discovery of low bandgap donor polymers. With the combination of low bandgap polymer donors and nonfullerene acceptors, solar cells with power conversion efficiencies (PCEs) over 16% were realized.<sup>[12,13]</sup> However, most research was conducted using spin-coated, small-area organic solar cells with active areas of some square centimeters only.<sup>[14–20]</sup> Toward commercialization of high-efficiency bulk-heterojunction (BHJ) organic solar cells, an upscaling of the thin film deposition process will be indispensable.<sup>[21,22]</sup> In this respect, printing

## 1. Introduction

Organic solar cells are of great interest in research and industry because their high mechanical flexibility, lightweight, and semi-transparency in combination with their ability to convert diffuse light into electrical energy enable many new applications, which were not possible so far with conventional silicon solar cells.

of active layers using meniscus-guided slot-die coating<sup>[23]</sup> was identified to be a promising approach as organic solar cell materials are solution-processible.<sup>[24,25]</sup> Printing enables a fast and low-cost large-area thin film deposition.<sup>[26–29]</sup> In addition, compared with spin coating, precursor solutions with lower concentrations are required for the printing of active layers,<sup>[30]</sup> which facilitates the use of high-efficiency materials suffering from poor solubility.

K. S. Wienhold, Dr. V. Körstgens, S. Grott, X. Jiang, Prof. P. Müller-Buschbaum  
Physik-Department  
Lehrstuhl für Funktionelle Materialien  
Technische Universität München  
James-Franck-Str. 1, 85748 Garching, Germany  
E-mail: muellerb@ph.tum.de

Dr. M. Schwartzkopf, Prof. S. V. Roth  
DESY  
Notkestraße 85, 22607 Hamburg, Germany

Prof. S. V. Roth  
Department of Fibre and Polymer Technology  
KTH  
Teknikringen 56-58, SE-100 44 Stockholm, Sweden

Prof. P. Müller-Buschbaum  
Heinz Maier-Leibnitz-Zentrum  
Technische Universität München  
Lichtenbergstr. 1, 85748 Garching, Germany

 The ORCID identification number(s) for the author(s) of this article can be found under <https://doi.org/10.1002/solr.202000086>.

© 2020 The Authors. Published by WILEY-VCH Verlag GmbH & Co. KGaA, Weinheim. This is an open access article under the terms of the Creative Commons Attribution License, which permits use, distribution and reproduction in any medium, provided the original work is properly cited.

DOI: 10.1002/solr.202000086

Moreover, printing is using the valuable materials more effectively as compared with spin coating in which most material is flung-off. Therefore, studying the slot-die coating process is an important step toward a real-world use of organic solar cells as the knowledge gained from research on spin-coated, small-area photovoltaic devices cannot simply be transferred to printed large-area devices.<sup>[21,31–33]</sup> So far, only a few studies were conducted to understand the process of slot-die coating and the drying kinetics of printed active layers for application in organic solar cells.<sup>[25,34–39]</sup> As most of these studies focused on the model system P3HT:PCBM or on other fullerene based systems, in situ studies on printing of nonfullerene based small molecule acceptors and high-efficiency polymers are not sufficiently provided. In particular, a fundamental understanding of the morphology formation is very limited today. Therefore, intensive research is needed to gain insights into the structure evolution during printing. Only based on such fundamental knowledge, further optimization of the printing process can be rationally done given the complexity of the non-equilibrium morphology of the BHJ structure which has a strong impact on the solar cell performance.<sup>[40–46]</sup> For this purpose, the conjugated low bandgap high-efficiency polymer donor poly[(2,6-(4,8-bis(5-(2-ethylhexylthio)-4-fluorothiophen-2-yl)-benzo[1,2-b:4,5-b']dithiophene))-*alt*-(5,5-(1',3'-di-2-thienyl-5',7'-bis(2-ethylhexyl)benzo[1',2'-c:4',5'-c']dithiophene-4,8-dione))], denoted PBDB-T-SF and the nonfullerene small molecule acceptor 3,9-bis(2-methylene-((3-(1,1-dicyanomethylene)-6,7-difluoro)-indanone))-5,5,11,11-tetrakis(4-hexylphenyl)-dithieno[2,3-d:2',3'-d']-s-indaceno[1,2-b:5,6-b']dithiophene, denoted IT-4F, which can achieve a PCE of about 13%<sup>[6,8]</sup> are printed out of chlorobenzene using meniscus-guided slot-die coating at ambient conditions. The morphological changes during solution deposition and subsequent drying of the thin film is studied in situ with grazing incidence small angle X-ray scattering (GISAXS), optical microscopy, and ultraviolet–visible (UV–vis) spectroscopy. The structure formation is followed from the initial wet to the final dry film and results are correlated to changing optical properties. Five regimes of morphology formation are identified by combining the results from the in situ GISAXS, optical microscopy, and UV–vis spectroscopy experiment.

## 2. Results and Discussion

### 2.1. In Situ Optical Microscopy

Active layers based on the conjugated donor polymer PBDB-T-SF and the nonfullerene small molecule acceptor IT-4F are printed out of chlorobenzene at room temperature at ambient

conditions. The slot-die-coated thin film is analyzed in situ with optical microscopy to follow the phase transition from the liquid state to the final dry film (**Figure 1**). Optical changes at the surface of the printed active layer are observed and five regimes of film formation are suggested from the large-scale structure evolution. During slot-die coating, a solution of PBDB-T-SF and IT-4F mixed in a 1:1 weight ratio in chlorobenzene is deposited on a microscopic glass slide. The initially deposited wet film exhibits a smooth surface without any distinct structure (**Figure 1a**). Within the first 140 s, no significant change occurs on the sample surface. Between 140 and 345 s after processing, slight waves evolve at the film surface (**Figure 1b**). The curvature is enhanced significantly within the time period between 345 and 460 s (**Figure 1c**). The film reaches a maximum of waviness before the solution is drawn back between 460 and 500 s. Drying occurs from the edges to the center of the substrate (**Figure 1d**). After 500 s, the slot-die-coated active layer appears completely dry and no optical changes occur anymore (**Figure 1e**). The final printed film is homogeneous on the length scales resolved with microscopy. The observation of surface waviness and the presence of different film formation regimes resemble findings from earlier in situ spin coating studies of thin polymer films although spin coating is the much faster process.<sup>[47]</sup> In an initial stage of spin coating just as for slot-die-coated thin films, a flat uniform surface was reported because a sufficient amount of solvent was present to completely dissolve the blend components. In the second regime, solvent evaporation provoked the formation of a heterogeneous solution and larger length scale structures about 100  $\mu\text{m}$  originating from Marangoni instabilities were observed during spin coating. After further solvent evaporation, a dry blend film resulted. Compared with spin-coated polymer films, on the mesoscopic scale printed active layers show a similar drying behavior even though five phases instead of three regimes can be distinguished and the time scales differ considerably.

### 2.2. In Situ UV–vis Spectroscopy

To further investigate the evolution of optical properties during printing of active layers based on PBDB-T-SF:IT-4F, in situ UV–vis spectroscopy is performed (**Figure 2**, **Figure S1a**, Supporting Information). A full absorbance spectrum is measured at different time steps to follow the transformation of the initial wet film (**Figure 2a**, black) to the final dry film (**Figure 2a**, green). During drying, the absorbance of the thin film clearly increases in the wavelength range between 580 and 720 nm, whereas it decreases significantly between 450 and 579 nm. The absorption onset of the active layer shifts continuously toward lower energies.

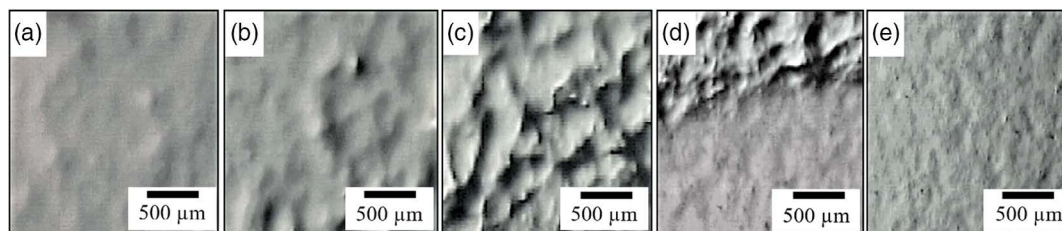


**Figure 1.** In situ optical microscopy of a slot-die-coated active layer based on PBDB-T-SF:IT-4F. Representative images are shown for different time periods after processing: a) 0–140 s; b) 140–345 s; c) 345–460 s; d) 460–500 s; e) 500–550 s.

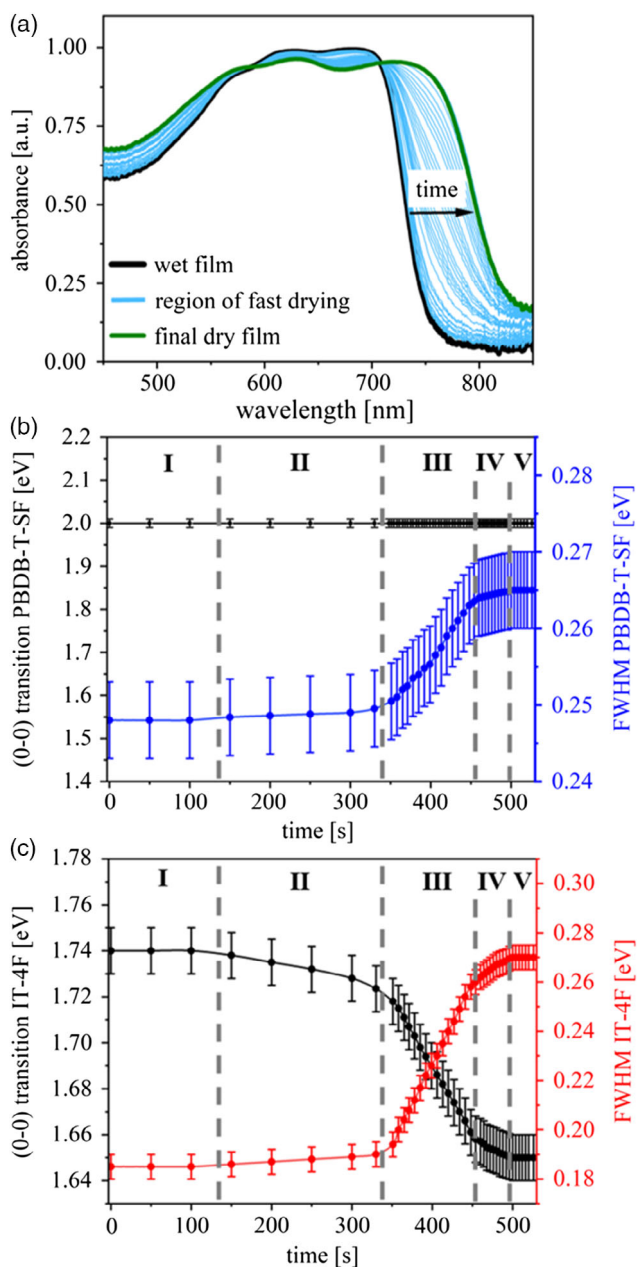


**Figure 2.** In situ UV-vis spectroscopy of a slot-die-coated active layer. For each time step, the absorbance spectrum is fitted with a set of Gaussian functions of equal width (Figure S4, Supporting Information). The broadening is applied equally to all Gaussian functions used in each new fit. Gaussian fits of the wet film and the final dry film are shown in Figure S4, Supporting Information. a) A continuous change in absorbance (bright blue) is observed during phase transition from the wet film (black) to the final dry film (green). b) For PBDB-T-SF, the energy corresponding to the (0–0) transition (black) and the FWHM of the Gaussian function (dark blue) are shown for different time steps during the drying process. c) For IT-4F, the evolution of the (0–0) transition (black) and the FWHM of the Gaussian function (red) are given during drying of the thin film.

The bandgap is determined with Tauc plot to be  $(1.63 \pm 0.04)$  eV in the initial wet film and  $(1.52 \pm 0.04)$  eV in the final dry film (Figure S2, Supporting Information) which resembles values

obtained for spin-coated thin films as well.<sup>[8]</sup> Within the first 345 s, only a slight change of absorbance can be observed in the UV-vis spectrum, whereas a pronounced change occurs between 345 and 460 s. Optical transitions are determined by modeling the absorbance data with fitting each UV-vis spectrum with a set of Gaussian functions, which all have the same width (Figure 3 and 4).<sup>[48]</sup> For PBDB-T-SF and IT-4F, absorbance spectra of a thin film and a dilute chlorobenzene solution are modeled with this approach to determine the electronic transitions of the polymer and the small molecule acceptor (Figure S3, Supporting Information). In a thin film based on a 1:1 ratio of PBDB-T-SF and IT-4F, the electronic transitions of both materials overlap and add up to a broad absorbance spectrum (Figure S4, Supporting Information). The UV-vis spectrum obtained for the final dry film has absorbance maxima at  $(630 \pm 5)$  nm and  $(730 \pm 5)$  nm (Figure 2a) and equals spectra obtained for spin-coated active layers.<sup>[49]</sup> The evolution of the (0–0) transition and the broadening of the full width at half maximum (FWHM) of the corresponding set of Gaussian functions are given for PBDB-T-SF (Figure 2b) and IT-4F (Figure 2c) for different time steps during printing. For each time step, the absorbance spectrum is fitted with a set of Gaussian functions of equal width. Then the next spectrum is fitted with a new set of Gaussian functions with different width for all the Gaussians simultaneously, i.e., the broadening is applied equally to all Gaussians used in each new fit. In agreement with the results obtained by in situ optical microscopy (Figure 1), five regimes of film formation can be observed (Figure 2b,c). In the initial wet film, no optical changes can be observed within the first 140 s. Between 140 and 345 s, the FWHM of PBDB-T-SF (Figure 2b, dark blue) and IT-4F (Figure 2c, red) broadens and a slight energy shift occurs for the (0–0) transition of IT-4F (Figure 2c, black), whereas the (0–0) transition of PBDB-T-SF (Figure 2b, black) does not change significantly during drying of the thin film. A significant change in absorbance (Figure 2a, bright blue) is observed between 345 and 460 s. The absorbance of the thin film decreases in the wavelength range between 580 and 720 nm, whereas it increases significantly between 450 and 579 nm. Within the region of fast drying, a significant broadening of the FWHM is measured for both PBDB-T-SF (Figure 2b, dark blue) and IT-4F (Figure 2c, red) and an energy shift of the (0–0) transition of IT-4F (Figure 2c, black) is observed. Between 460 and 500 s, the FWHM of PBDB-T-SF and IT-4F as well as the (0–0) transition of IT-4F in the almost dry film shift slightly. After 500 s, the optical properties of the thin film are stable and no further change can be observed.

**Table 1** shows the electronic transitions for the conjugated polymer and the small molecule acceptor in a slot-die-coated active layer for the initial wet film and the final dry film. The (0–0) transition of IT-4F is clearly red-shifted from  $(1.73 \pm 0.01)$  eV to  $(1.67 \pm 0.03)$  eV, an effect which is well known for many small molecule acceptors.<sup>[50,51]</sup> The (0–1) transition does not shift significantly whereas the (0–2) and (0–3) transitions are blue-shifted from  $(1.92 \pm 0.01)$  to  $(2.03 \pm 0.03)$  eV and from  $(2.01 \pm 0.01)$  to  $(2.22 \pm 0.02)$  eV. The width of the set of Gaussian functions increases from  $(0.185 \pm 0.005)$  to  $(0.270 \pm 0.005)$  eV during drying, implying an increase in disorder in the active layer.<sup>[48,52]</sup> We assume that this increase in disorder originates from the formation of different domain sizes in the bulk-heterojunction layer, different arrangement of polymer chains depending on the

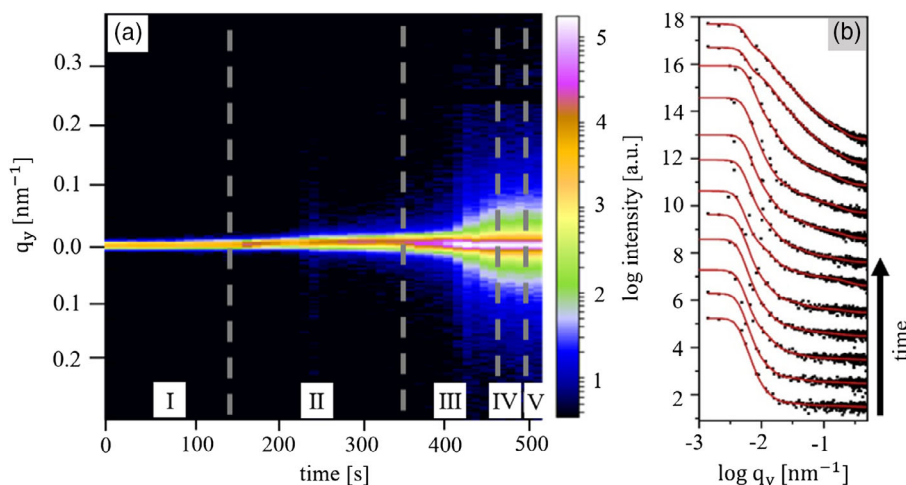


**Figure 3.** In situ GISAXS follows the morphology change during drying of a slot-die-coated thin film of PBDB-T-SF:IT-4F. a) Color mapping of the horizontal line cuts performed at the critical angle of the polymer over time shows the five regimes of film formation. b) Stacking of horizontal line cuts (black dots) and modeling results (red lines) from the initial wet film (bottom) to the final dry film (top) by applying a model based on the DWBA and the LMA. Data are shifted along the intensity axis for clarification.

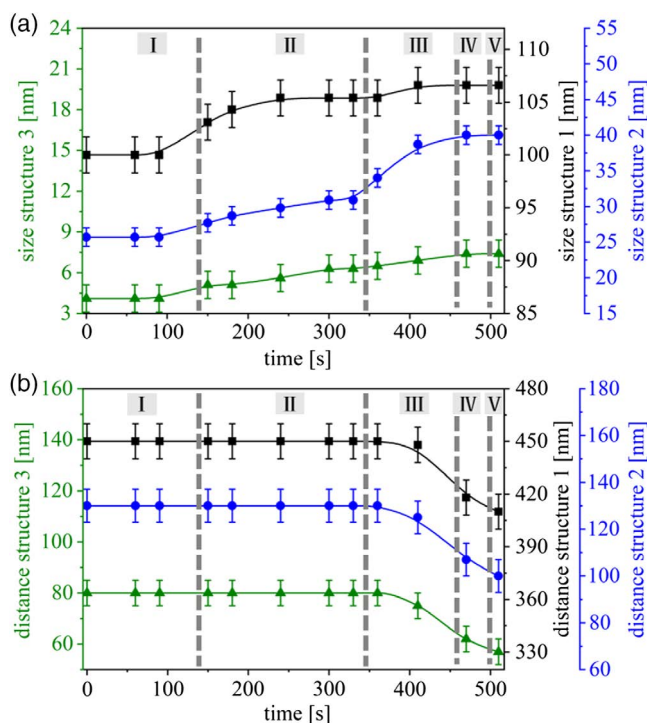


**Figure 4.** a) Average structure sizes and b) distances obtained from modeling the horizontal line cuts of the in situ GISAXS experiment. The structure evolution occurring during the in situ GISAXS experiment is shown for the largest (black squares), medium (blue circles), and smallest (green triangles) polymer substructure. The error bars give an estimate about the fit precision and give a range in which the fit still describes the data. Five regimes of film formation can be distinguished and marked with I–V. Splines are guides to the eye.

surrounding molecules, and a strong interaction between the polymer and acceptor molecules. In contrast, in a solution, the

active materials mainly interact with solvent molecules. During drying of PBDB-T-SF, no significant shift of electronic transitions is observed. The absence of any pronounced bathochromic shift is due to a very effective aggregation of polymer chains in the precursor solution.<sup>[53–55]</sup> This effect results from the fluorination of the polymer which provokes F–H and F–S interactions.<sup>[8,53]</sup> The strong intermolecular  $\pi$ – $\pi$  stacking in the dry film is expected to effectuate improved charge transport between polymer molecules, but lowers the solubility of PBDB-T-SF. To minimize unfavorable solvent–polymer interactions, aggregates are formed in the solution and facilitate the nanophase separation and the formation of a BHJ structure in the printed active layer.<sup>[56–58]</sup> Just as for the acceptor, the width of the set of Gaussian functions for the donor polymer is broadening during the drying. The width changes from  $(0.250 \pm 0.005)$  eV in the wet film to  $(0.265 \pm 0.005)$  eV in the final dry film which indicates an increasing disorder in the polymer domains during drying of the thin film.<sup>[52]</sup> The energy shift of electronic transitions together with an increase in the width of the set of Gaussian functions provoke an overall broadening of the absorbance spectrum as well as a shift of the bandgap toward lower energies. In contrast to the five regimes observed for slot-die-coated PBDB-T-SF:IT-4F films in the present study, only three phases of structure formation were reported for P3HT:PCBM thin films during wet chemical deposition with doctor blading.<sup>[59,60]</sup> Wang et al. followed the evolution of the extinction coefficient with in situ ellipsometry.<sup>[59]</sup> Within the first phase, the absorbance spectra resembled the spectrum of a dilute solution, which is in agreement with our findings. In the second drying phase, a significant red-shift of the absorbance was observed and the extinction coefficient increased. In the present study, for printed PBDB-T-SF:IT-4F, this regime is further subclassified as the observed optical changes in thin PBDB-T-SF:IT-4F films occur with different velocities. In the third phase described for P3HT:PCBM, the drying slowed down until the thin film has fully solidified, whereas in the present work, the last regime is defined to be the final dry film only.

**Table 1.** Electronic transitions of IT-4F and PBDB-T-SF during drying of the slot-die-coated thin film.

Material	IT-4F	IT-4F	IT-4F	IT-4F	PBDB-T-SF	PBDB-T-SF	PBDB-T-SF	PBDB-T-SF
Order of transition	0–0	0–1	0–2	0–3	0–0	0–1	0–2	0–3
Transition in wet film [eV]	1.74 ± 0.01	1.83 ± 0.01	1.92 ± 0.01	2.01 ± 0.02	2.00 ± 0.01	2.14 ± 0.01	2.28 ± 0.02	2.42 ± 0.02
Transition in dry film [eV]	1.65 ± 0.02	1.84 ± 0.02	2.03 ± 0.02	2.22 ± 0.02	2.00 ± 0.01	2.15 ± 0.01	2.30 ± 0.02	2.45 ± 0.02

In addition to these studies, for spin-coated thin films based on P3HT:PCBM, the evolution of absorbance was followed with in situ UV–vis spectroscopy as well.<sup>[60]</sup> In the first stage, a reduction of absorbance due to ejection of solution was reported. In the second stage, a steady state was reached. The solvent evaporation was ongoing, but did not change the solution state of P3HT. In the third stage, the thin film was in a solid state and the absorbance increased until a plateau was reached. Even though the drying phases observed for doctor bladed or spin-coated P3HT:PCBM and slot-die-coated PBDB-T-SF:IT-4F differ, all film formation processes show a red-shift and broadening of the absorbance spectra. This is very favorable for application in organic solar cells as the solar spectrum can be exploited more efficiently.

### 2.3. In Situ GISAXS

The kinetics of the inner morphology formation of a slot-die-coated active layer (Figure S1b, Supporting Information) is probed via GISAXS with high statistical significance and time resolution.<sup>[61,62]</sup> Horizontal line cuts of the 2D GISAXS data are performed at the critical angle of PBDB-T-SF (Yoneda region) to trace the evolution during the in situ experiment (Figure 3). Average structure sizes and the corresponding average distances between the polymer domains can be obtained by modeling the horizontal line cuts with a model based on the effective interface approximation of the distorted wave Born approximation (DWBA) and the local monodisperse approximation (LMA).<sup>[63–65]</sup> In this model, polymer domains are described as cylindrical structures which is a common approach in polymer physics to describe polymer thin films.<sup>[45,66,67]</sup> Figure 3b shows the data points obtained from the scattering experiments (black dots) as well as the modeling results (red line) from the beginning (bottom) to the end of the drying process (top). The structure parameters are obtained by modeling the horizontal line cuts with three substructures (Figure 4). For the organic solar cell performance, the medium structure size (Figure 4, blue) in the range of about  $(40 \pm 1)$  nm for the final dry film is most relevant as it fits typical exciton diffusion lengths.<sup>[68,69]</sup> In the vertical line cuts of the 2D GISAXS data, no characteristic scattering signal of correlated roughness<sup>[70–72]</sup> is observed (Figure S6a, Supporting Information). Thus, along the surface normal no correlated enrichment layers are present. In the in situ GISAXS experiment, five regimes of film formation, which are in agreement with the phases determined with in situ UV–vis spectroscopy, are distinguished (Figure 4 and 5). In the initial time period after processing, the wet film shows no significant morphological change within the first 140 s. However, some polymer agglomerates already exist in the very beginning (Figure 4a and 5, blue cylinders) and solvent molecules evaporate (Figure 5, golden spheres). Structure sizes

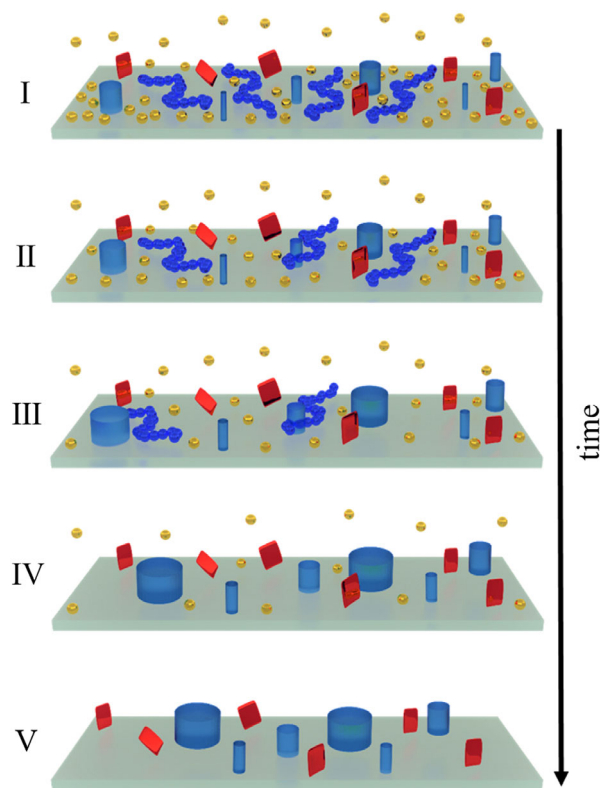


**Figure 5.** Schematic of the structure evolution during the drying of the printed active layer with time (from top to bottom) showing selected building blocks from the active layer morphology. Three polymer substructures (blue cylinders), polymer chains in solution (blue chains), the small molecule acceptor (red cuboids), and solvent molecules (golden spheres), which evaporate during the drying process, are shown. Five stages of drying are illustrated. (I) Some polymer domains already exist in the beginning and solvent molecules evaporate. (II) Domains grow by attaching of polymer chains. (III) A distinct structure change and evaporation of solvent occurs. (IV) Polymer domains stop to grow and average distances are reduced. (V) The final dry film with stable morphology can be observed.

are about  $(100 \pm 2)$  nm for the largest (Figure 4a, black),  $(26 \pm 1)$  nm for the medium (Figure 4a, blue) and  $(4 \pm 1)$  nm for the smallest structure (Figure 4a, green). The corresponding distances are about  $(450 \pm 10)$  nm,  $(130 \pm 7.0)$  nm, and  $(80 \pm 5.0)$  nm (Figure 4b). Between 140 and 345 s after thin film deposition, polymer chains in solution start to be integrated in the cylindrical shaped polymer domains (Figure 5, blue chains and cylinders). In this region, the three substructures grow slowly and reach average domain sizes of  $(105 \pm 1)$  nm,  $(31 \pm 1)$  nm, and  $(6 \pm 1)$  nm, whereas the average distances do not change

(Figure 4 and 5). In the third region which occurs between 345 and 460 s, a distinct and fast growth of structures is visible, whereas the average distances do not change significantly (Figure 4 and 5). The average structure sizes grow to  $(107 \pm 1)$  nm for the largest,  $(40 \pm 1)$  nm for the medium, and  $(7 \pm 1)$  nm for the smallest domain size. In the fourth region which occurs between 460 and 500 s, the thin film is almost dry and structures stop to grow (Figure 4a, and 5). Within this region of drying, the residual solvent evaporates provoking a compaction<sup>[73,74]</sup> of the thin film and a reduction of the average distances to  $(410 \pm 8)$  nm,  $(100 \pm 7)$  nm, and  $(57 \pm 5)$  nm for large, medium, and small structures (Figure 4b).

In the final region, which occurs after 500 s, the thin film is completely dry and the average domain sizes and corresponding distances are stable (Figure 4 and 5). The dry film morphology of the slot-die-coated thin PBDB-T-SF:IT-4F films with structure sizes of some tens of nanometers is in agreement with structure sizes observed with AFM at the surface of spin-coated thin films, although the largest structure size is not reported in the earlier work.<sup>[8]</sup> In previous studies on printed thin films based on different materials, three or five phases of structure formation were reported from in situ GISAXS and grazing incidence X-ray diffraction (GIXD) experiments. For example, in case of active layers based on DPPBT:PCBM, only three regimes were distinguished.<sup>[37]</sup> In the first phase, the material was well dissolved. In the second phase, the solvent evaporated quickly provoking polymer aggregation. In the third phase, further aggregation, formation of fibrils, and quick crystallization occurred until the final morphology was reached. For doctor bladed thin films based on pBTT-C14:PCBM, five regimes were observed, which differ from the five phases observed for slot-die-coated PBDB-T-SF:IT-4F films.<sup>[75]</sup> In the first phase, the solvent evaporated quickly, whereas the solubility limit was increased by the remaining solvent additive. In the second phase, the interlamellar spacing decreased and the crystallinity increased, whereas the distances observed in PBDB-T-SF:IT-4F were constant in this regime. In the third phase, the solvent additive evaporated and further crystallization occurred, whereas for PBDB-T-SF:IT-4F a rapid growth of amorphous domains was reported. In the fourth phase, the backbone spacing decreased, resulting in a denser packing of the polymer, which resembled the observed decrease in distances in thin PBDB-T-SF:IT-4F-based films. In the fifth phase, the film was dry and no further change of morphology happened. In addition, also for slot-die-coated P3HT:PCBM, five regimes were distinguished with GISAXS, which again differ in the details from the five phases observed for pBTT-C14:PCBM or PBDB-T-SF:IT-4F.<sup>[25]</sup> The first phase was described as a well-dissolved state. In the second phase, the domain radius increased slowly, whereas a fast decrease in distances was observed. In contrast, for PBDB-T-SF:IT-4F, distances did not change in this regime. In the third phase, a rapid structure growth and slight increase in distances happened, which is in contrast to the constant distances observed in the printing of PBDB-T-SF:IT-4F and pBTT-C14:PCBM. In the fourth phase, a further structure growth was observed and the distances were constant, whereas no structure growth but a decrease in distances is observed for the other systems. In the last phase, the thin film was dry and stable. Therefore, the observed stages of structure formation differ significantly for different material

systems, indicating that knowledge gained from one system cannot simply be transferred to another system.

#### 2.4. Combining In Situ Optical Microscopy, UV-vis Spectroscopy, and GISAXS Results

In the in situ optical microscopy, UV-vis spectroscopy, and the GISAXS experiment, five regimes of film formation can be observed. Five stages were already reported for printing of P3HT:PCBM thin films.<sup>24</sup> In the initial time period after processing, the slot-die-coated thin film is wet and no significant change of optical properties (Figure 1 and 2) or morphology (Figure 4) occurs within the first 140 s. Between 140 and 345 s, the average structure sizes of the polymer domains start to grow slowly (Figure 4a), the absorbance of the thin film changes (Figure 2), and the surface waviness (Figure 1b) increases simultaneously. In the third region of drying which occurs between 345 and 460 s, a distinct and fast growth of nanostructures can be observed (Figure 4a) which provokes a very pronounced change of optical properties in the active layer (Figure 2). The bandgap of the active layer clearly red-shifts from  $(1.63 \pm 0.04)$  eV to  $(1.52 \pm 0.04)$  eV and a shift of energy level occurs (Table 1, Figure S2, Supporting Information). Data modeling with sets of Gaussian functions shows a broadening of the width for the polymer and the acceptor (Figure 2b,c) which indicates an increase in disorder in the active layer.<sup>[52]</sup> In addition, distinct waves are visible at the sample surface (Figure 1c). Between 460 and 500 s, the average distances between the polymer domains are reduced (Figure 4b) in the almost dry film and a withdrawal of solution from the edges to the center of the substrate is visible in the optical microscopy (Figure 1d). A slight change in the FWHM can be observed for PBDB-T-SF and IT-4F as well as a shift of the (0-0) transition of IT-4F (Figure 2b,c). After 500 s, the slot-die-coated active layer is dry and the morphology and optical properties are stable. Thus, the structure formation of PBDB-T-SF:IT-4F films during slot-die coating differs from that reported in earlier studies performed on other material systems. Therefore, new and promising materials need to be studied individually to understand their structure formation process, which will be the prerequisite to further optimize the printing process and the device performance.

### 3. Conclusion

Slot-die coating of thin films based on PBDB-T-SF:IT-4F for application as active layers in high-efficiency organic solar cells is studied in situ with GISAXS, UV-vis spectroscopy, and optical microscopy from the initial wet film to the final dry film state. Combining results from GISAXS and UV-vis spectroscopy, the morphological evolution of PBDB-T-SF:IT-4F is correlated to changing absorbance behavior. We identify five regimes of film formation, which share similarity with earlier studies on printed active layers of DPPBT:PCBM and P3HT:PCBM. However, the details of the film formation are system specific in particular concerning the temporal evolution of interdomain distances. During the drying process, polymer domains with a size about 40 nm are formed in the active layer. As this structure size fits

typical exciton diffusion lengths, a favorable effect on the solar cell performance is expected. Similar nanoscale structures were observed as well in spin-coated PBDB-T-SF:IT-4F films, which demonstrates that with slot-die coating well-suited BHJ structures can be prepared as well after optimization of the printing parameters. A red-shift of the optical bandgap and an overall broadening of the absorbance spectra are observed during drying which allows exploiting the sun emission spectrum more efficiently. The in situ experiments presented in this work provide insights into the evolution of the active layer's morphology and optical properties which have a high impact on the device performance and are an important step toward further optimization and upscaling of the solar cell production.

## 4. Experimental Section

**Materials:** Poly[(2,6-(4,8-bis(5-(2-ethylhexylthio)-4-fluorothiophen-2-yl)-benzo[1,2-b:4,5-b']dithiophene))-alt-(5,5-(1',3'-di-2-thienyl-5',7'-bis(2-ethylhexyl)benzo[1',2'-c:4',5'-c']dithiophene-4,8-dione)] (PBDB-T-SF) and 3,9-bis(2-methylene-((3-(1,1-dicyanomethylene)-6,7-difluoro-indanone))-5,5,11,11-tetrakis(4-hexylphenyl)-dithieno[2,3-d:2',3'-d']-s-indaceno[1,2-b:5,6-b']dithiophene (IT-4F) were purchased from Solarmer. PBDB-T-SF and IT-4F were mixed in a 1:1 weight ratio, dissolved in chlorobenzene (Merck) and stirred at 100 °C for 48 h. For all experiments, microscope slides (Carl Roth) with a size of 7.6 cm × 2.6 cm were cleaned with acid and used as substrates for slot-die coating of the active layers. For the cleaning procedure, a mixture of 50 mL deionized H<sub>2</sub>O, 80 mL H<sub>2</sub>O<sub>2</sub> (Carl Roth) and 180 mL H<sub>2</sub>SO<sub>4</sub> (Carl Roth) were heated to 80 °C to clean the glass slides for 15 min. All substrates were rinsed with deionized water to completely remove the cleaning components and dried with N<sub>2</sub>.

**Optical Microscopy:** In situ optical microscopy was carried out with a MINTRON 62VIP video microscope and a PHOTONIC Optics PL3000 lamp. The optical microscope was installed above the slot-die coater to enable a top view on the sample surface. The optics was focused on the center of the substrate before slot-die coating at room temperature and ambient conditions. The complete printing procedure and film formation process were recorded as a video and converted to individual images after the measurement with a second time resolution. For every region of drying, one characteristic image is shown.

**UV-vis Spectroscopy:** A MBB1D1 broadband light-emitting diode from THORLABS was installed at the bottom plate of the slot-die coater below the sample holder to measure in situ UV-vis spectroscopy in transmission mode. The transmitted light was coupled into a CAS 140 CT Instrument Systems Compact Array spectrometer using a glass fiber. A full UV-vis spectrum was measured every 10 s to follow the process of drying and the evolution of the optical transmittance in situ. The experiment was conducted at room temperature and ambient conditions. All windows of the slot-die coater were masked with aluminum foil before performing the in situ UV-vis spectroscopy experiment to reduce the contribution of ambient scattering light.

**GISAXS:** The GISAXS experiment was performed at the beamline P03<sup>[76]</sup> at the PETRA III synchrotron source at DESY, Hamburg, with a sample-detector-distance of 3176 mm and a wavelength of 0.09763 nm. The incidence angle was aligned to 0.35°. The scattering signal was detected by a Dectris Pilatus 1M detector. The exposure time per frame was 0.1 s with a waiting time of 9.9 s between two frames to ensure to stay below the critical dose for radiation damage and to rule out the possibility of morphological changes caused by the high brilliance of the X-ray beam (Figure S5 and S6, Supporting Information).

Directly Programmable Data Analysis Kit (DPDAK),<sup>[77]</sup> an open source Python-based program, was used for data analysis and calibration (sample-detector distance, beam center). The critical angle of PBDB-T-SF (Yoneda region) was calculated to be 0.11° for the used X-ray energy of 12.7 keV.

## Supporting Information

Supporting Information is available from the Wiley Online Library or from the author.

## Acknowledgements

The authors acknowledge funding from Deutsche Forschungsgemeinschaft (DFG, German Research Foundation) under Germany's Excellence Strategy—EXC 2089/1—390776260 (e-conversion) and via International Research Training Group 2022 Alberta/Technical University of Munich International Graduate School for Environmentally Responsible Functional Materials (ATUMS) as well as from TUM.solar in the context of the Bavarian Collaborative Research Project “Solar Technologies Go Hybrid” (SolTech) and the Center for NanoScience (CeNS). K.S.W. acknowledges the Hans Böckler Stiftung and X.J. the China Scholarship Council (CSC) funding. In situ GISAXS experiments were conducted at the light source PETRA III at DESY, a member of the Helmholtz Association (HGF).

## Conflict of Interest

The authors declare no conflict of interest.

## Keywords

GISAXS, in situ printing, low bandgap polymers, nonfullerene acceptors, slot-die coating

Received: February 12, 2020

Revised: April 5, 2020

Published online:

- [1] M. B. Schubert, J. H. Werner, *Mater. Today* **2006**, *9*, 42.
- [2] S. Berny, N. Blouin, A. Distler, H.-J. Egelhaaf, M. Krompiec, A. Lohr, O. R. Lozman, G. E. Morse, L. Nanson, A. Pron, T. Sauermann, N. Seidler, S. Tierney, P. Tiwana, M. Wagner, H. Wilson, *Adv. Sci.* **2016**, *3*, 1500342.
- [3] Z. Zhang, Z. Yang, J. Deng, Y. Zhang, G. Guan, H. Peng, *Small* **2015**, *11*, 675.
- [4] T. Sano, S. Inaba, V. Vohra, *ACS Appl. Energy Mater.* **2019**, *2*, 2534.
- [5] P. Gangwar, N. M. Kumar, A. K. Singh, A. Jayakumar, M. Mathew, *Case Stud. Therm. Eng.* **2019**, *14*, 100474.
- [6] J. Hou, O. Inganäs, R. H. Friend, F. Gao, *Nat. Mater.* **2018**, *17*, 119.
- [7] H. Feng, Y.-Q.-Q. Yi, X. Ke, J. Yan, Y. Zhang, X. Wan, C. Li, N. Zheng, Z. Xie, Y. Chen, *Adv. Energy Mater.* **2019**, *9*, 1803541.
- [8] W. Zhao, S. Li, H. Yao, S. Zhang, Y. Zhang, B. Yang, J. Hou, *J. Am. Chem. Soc.* **2017**, *139*, 7148.
- [9] H. Fu, Z. Wang, Y. Sun, *Angew. Chem.* **2019**, *58*, 4442.
- [10] H. Sun, Y. Tang, C. W. Koh, S. Ling, R. Wang, K. Yang, J. Yu, Y. Shi, Y. Wang, H. Y. Woo, X. Guo, *Adv. Mater.* **2019**, *31*, e1807220.
- [11] G. Li, Q. Xu, C. Chang, Q. Fan, X. Zhu, W. Li, X. Guo, M. Zhang, W.-Y. Wong, *Macromol. Rapid Commun.* **2019**, *40*, e1800660.
- [12] B. Fan, D. Zhang, M. Li, W. Zhong, Z. Zeng, L. Ying, F. Huang, Y. Cao, *Sci. China Chem.* **2019**, *62*, 746.
- [13] J. Yuan, Y. Zhang, L. Zhou, G. Zhang, H.-L. Yip, T.-K. Lau, X. Lu, C. Zhu, H. Peng, P. A. Johnson, M. Leclerc, Y. Cao, J. Ulanski, Y. Li, Y. Zou, *Joule* **2019**, *3*, 1140.
- [14] L. Dou, J. Gao, E. Richard, J. You, C.-C. Chen, K. C. Cha, Y. He, G. Li, Y. Yang, *J. Am. Chem. Soc.* **2012**, *134*, 10071.

- [15] D. Yang, Q. Yang, L. Yang, Q. Luo, Y. Chen, Y. Zhu, Y. Huang, Z. Lu, S. Zhao, *Chem. Commun.* **2014**, 50, 9346.
- [16] X. Shi, J. Chen, K. Gao, L. Zuo, Z. Yao, F. Liu, J. Tang, A. K.-Y. Jen, *Adv. Energy Mater.* **2018**, 8, 1702831.
- [17] Y. Yang, Z.-G. Zhang, H. Bin, S. Chen, L. Gao, L. Xue, C. Yang, Y. Li, *J. Am. Chem. Soc.* **2016**, 138, 15011.
- [18] M. H. Hoang, G. E. Park, S. Choi, C. G. Park, S. H. Park, T. van Nguyen, S. Kim, K. Kwak, M. J. Cho, D. H. Choi, *J. Mater. Chem. C* **2019**, 7, 111.
- [19] O. K. Kwon, J.-H. Park, D. W. Kim, S. K. Park, S. Y. Park, *Adv. Mater.* **2015**, 27, 1951.
- [20] J. Zhou, Y. Zuo, X. Wan, G. Long, Q. Zhang, W. Ni, Y. Liu, Z. Li, G. He, C. Li, B. Kan, M. Li, Y. Chen, *J. Am. Chem. Soc.* **2013**, 135, 8484.
- [21] I. Burgués-Ceballos, M. Stella, P. Lacharmoise, E. Martínez-Ferrero, *J. Mater. Chem. A* **2014**, 2, 17711.
- [22] T. R. Andersen, H. F. Dam, M. Hösel, M. Helgesen, J. E. Carlé, T. T. Larsen-Olsen, S. A. Gevorgyan, J. W. Andreasen, J. Adams, N. Li, F. Machui, G. D. Spyropoulos, T. Ameri, N. Lemaître, M. Legros, A. Scheel, D. Gaiser, K. Kreul, S. Berny, O. R. Lozman, S. Nordman, M. Välimäki, M. Viikman, R. R. Søndergaard, M. Jørgensen, C. J. Brabec, F. C. Krebs, *Energy Environ. Sci.* **2014**, 7, 2925.
- [23] S. Pröllner, D. Moseguí González, C. Zhu, E. Schaible, C. Wang, P. Müller-Buschbaum, A. Hexemer, E. M. Herzig, *Rev. Sci. Instrum.* **2017**, 88, 66101.
- [24] H. W. Ro, J. M. Downing, S. Engmann, A. A. Herzing, D. M. DeLongchamp, L. J. Richter, S. Mukherjee, H. Ade, M. Abdelsamie, L. K. Jagadamma, A. Amassian, Y. Liu, H. Yan, *Energy Environ. Sci.* **2016**, 9, 2835.
- [25] S. Pröllner, F. Liu, C. Zhu, C. Wang, T. P. Russell, A. Hexemer, P. Müller-Buschbaum, E. M. Herzig, *Adv. Energy Mater.* **2016**, 6, 1501580.
- [26] H.-C. Cha, Y.-C. Huang, F.-H. Hsu, C.-M. Chuang, D.-H. Lu, C.-W. Chou, C.-Y. Chen, C.-S. Tsao, *Sol. Energy Mater. Sol. Cells* **2014**, 130, 191.
- [27] Y. Galagan, H. Fledderus, H. Gorter, H. H. 't Mannelte, S. Shanmugam, R. Mandamparambil, J. Bosman, J.-E. J. M. Rubingh, J.-P. Teunissen, A. Salem, I. G. de Vries, R. Andriessen, W. A. Groen, *Energy Technol.* **2015**, 3, 834.
- [28] M. Helgesen, J. E. Carlé, F. C. Krebs, *Adv. Energy Mater.* **2013**, 3, 1664.
- [29] D. Vak, K. Hwang, A. Faulks, Y.-S. Jung, N. Clark, D.-Y. Kim, G. J. Wilson, S. E. Watkins, *Adv. Energy Mater.* **2015**, 5, 1401539.
- [30] J. Bergqvist, S. A. Mauger, K. Tvingstedt, H. Arwin, O. Inganäs, *Sol. Energy Mater. Sol. Cells* **2013**, 114, 89.
- [31] S. Hong, J. Lee, H. Kang, K. Lee, *Sol. Energy Mater. Sol. Cells* **2013**, 112, 27.
- [32] J. Peet, M. L. Senatore, A. J. Heeger, G. C. Bazan, *Adv. Mater.* **2009**, 21, 1521.
- [33] K. Zhao, H. Hu, E. Spada, L. K. Jagadamma, B. Yan, M. Abdelsamie, Y. Yang, L. Yu, R. Munir, R. Li, G. O. N. Ndjawa, A. Amassian, *J. Mater. Chem. A* **2016**, 4, 16036.
- [34] A. P. L. Böttiger, M. Jørgensen, A. Menzel, F. C. Krebs, J. W. Andreasen, *J. Mater. Chem.* **2012**, 22, 22501.
- [35] Y.-R. Chang, H.-M. Chang, C.-F. Lin, T.-J. Liu, P.-Y. Wu, *J. Colloid Interface Sci.* **2007**, 308, 222.
- [36] X. Gu, J. Reinspach, B. J. Worfolk, Y. Diao, Y. Zhou, H. Yan, K. Gu, S. Mannsfeld, M. F. Toney, Z. Bao, *ACS Appl. Energy Mater.* **2016**, 8, 1687.
- [37] F. Liu, S. Ferdous, E. Schaible, A. Hexemer, M. Church, X. Ding, C. Wang, T. P. Russell, *Adv. Mater.* **2015**, 27, 886.
- [38] A. J. Pearson, T. Wang, A. D. F. Dunbar, H. Yi, D. C. Watters, D. M. Coles, P. A. Staniec, A. Iraqi, R. A. L. Jones, D. G. Lidzey, *Adv. Funct. Mater.* **2014**, 24, 659.
- [39] C. M. Palumbiny, F. Liu, T. P. Russell, A. Hexemer, C. Wang, P. Müller-Buschbaum, *Adv. Mater.* **2015**, 27, 3391.
- [40] C. J. Brabec, S. Gowrisanker, J. J. M. Halls, D. Laird, S. Jia, S. P. Williams, *Adv. Mater.* **2010**, 22, 3839.
- [41] Y. Gu, C. Wang, T. P. Russell, *Adv. Energy Mater.* **2012**, 2, 683.
- [42] M. Kim, J.-H. Kim, H. H. Choi, J. H. Park, S. B. Jo, M. Sim, J. S. Kim, H. Jinnai, Y. D. Park, K. Cho, *Adv. Energy Mater.* **2014**, 4, 1300612.
- [43] F. Liu, W. Zhao, J. R. Tumbleston, C. Wang, Y. Gu, D. Wang, A. L. Briseno, H. Ade, T. P. Russell, *Adv. Energy Mater.* **2014**, 4, 1301377.
- [44] C. McDowell, M. Abdelsamie, K. Zhao, D.-M. Smilgies, G. C. Bazan, A. Amassian, *Adv. Energy Mater.* **2015**, 5, 1501121.
- [45] C. J. Schaffer, C. M. Palumbiny, M. A. Niedermeier, C. Jendrzewski, G. Santoro, S. V. Roth, P. Müller-Buschbaum, *Adv. Mater.* **2013**, 25, 6760.
- [46] J. R. Tumbleston, B. A. Collins, L. Yang, A. C. Stuart, E. Gann, W. Ma, W. You, H. Ade, *Nat. Photon.* **2014**, 8, 385.
- [47] S. Ebbens, R. Hodgkinson, A. J. Parnell, A. Dunbar, S. J. Martin, P. D. Topham, N. Clarke, J. R. Howse, *ACS Nano* **2011**, 5, 5124.
- [48] S. T. Hoffmann, H. Bässler, A. Köhler, *J. Phys. Chem. B* **2010**, 114, 17037.
- [49] L. He, C. Wan, H. Dong, X. Zhang, J. Huang, *IEEE J. Photovoltaics* **2019**, 9, 1290.
- [50] M. Chang, Y. Wang, Y.-Q.-Q. Yi, X. Ke, X. Wan, C. Li, Y. Chen, *J. Mater. Chem. A* **2018**, 6, 8586.
- [51] B. Kan, H. Feng, H. Yao, M. Chang, X. Wan, C. Li, J. Hou, Y. Chen, *Sci. China Chem.* **2018**, 61, 1307.
- [52] A. W. Götz, J. I. Rodríguez, F. L. Castillo-Alvarado, D. E. Trujillo-González, *Int. J. Quantum Chem.* **2019**, 352, e25883.
- [53] Z. Du, X. Bao, Y. Li, D. Liu, J. Wang, C. Yang, R. Wimmer, L. W. Städe, R. Yang, D. Yu, *Adv. Energy Mater.* **2018**, 8, 1701471.
- [54] W. W. H. Wong, J. Subbiah, S. R. Puniredd, W. Pisula, D. J. Jones, A. B. Holmes, *Polym. Chem.* **2014**, 5, 1258.
- [55] J. Ma, G. Feng, F. Liu, F. Yang, Y. Guo, Y. Wu, W. Li, *Dyes Pigment.* **2019**, 165, 335.
- [56] M. Chang, J. Lee, N. Kleinhenz, B. Fu, E. Reichmanis, *Adv. Funct. Mater.* **2014**, 24, 4457.
- [57] M. Chang, D. Choi, G. Wang, N. Kleinhenz, N. Persson, B. Park, E. Reichmanis, *ACS Appl. Mater. Interfaces* **2015**, 7, 14095.
- [58] G. Jo, J. Jung, M. Chang, *Polymers* **2019**, 11, 332.
- [59] T. Wang, A. D. F. Dunbar, P. A. Staniec, A. J. Pearson, P. E. Hopkinson, J. E. MacDonald, S. Lilliu, C. Pizzey, N. J. Terrill, A. M. Donald, A. J. Ryan, R. A. L. Jones, D. G. Lidzey, *Soft Matter* **2010**, 6, 4128.
- [60] M. Abdelsamie, K. Zhao, M. R. Niazi, K. W. Chou, A. Amassian, *J. Mater. Chem. C* **2014**, 2, 3373.
- [61] P. Müller-Buschbaum, *Anal. Bioanal. Chem.* **2003**, 376, 3.
- [62] G. Renaud, R. Lazzari, F. Leroy, *Surf. Sci. Rep.* **2009**, 64, 255.
- [63] M. Stamm, *Polymer Surfaces and Interfaces: Characterization, Modification and Applications*, Springer, Berlin **2007**.
- [64] M. Gomez, A. Nogales, M. C. Garcia-Gutierrez, T. A. Ezquerra, *Applications of Synchrotron Light to Scattering and Diffraction in Materials and Life Sciences*, Springer, Berlin, Heidelberg **2009**.
- [65] M. A. Ruderer, P. Müller-Buschbaum, *Soft Matter* **2011**, 7, 5482.
- [66] C. J. Schaffer, J. Schlipf, E. Dwi Indari, B. Su, S. Bernstorff, P. Müller-Buschbaum, *ACS Appl. Mater. Interfaces* **2015**, 7, 21347.

- [67] D. Yang, F. C. Löhner, V. Körstgens, A. Schreiber, S. Bernstorff, J. M. Buriak, P. Müller-Buschbaum, *ACS Energy Lett.* **2019**, *4*, 464.
- [68] A. J. Heeger, *Adv. Mater.* **2014**, *26*, 10.
- [69] H. Hoppe, N. S. Sariciftci, *J. Mater. Chem.* **2006**, *16*, 45.
- [70] V. Holy, T. Baumbach, *Phys. Rev. B* **1994**, *49*, 10668.
- [71] P. Müller-Buschbaum, M. Stamm, *Macromolecules* **1998**, *31*, 3686.
- [72] J. J. van Franeker, D. Hermida-Merino, C. Gommès, K. Arapov, J. J. Michels, R. A. J. Janssen, G. Portale, *Adv. Funct. Mater.* **2017**, *27*, 1702516.
- [73] S. V. Roth, G. Herzog, V. Körstgens, A. Buffet, M. Schwartzkopf, J. Perlich, M. M. Abul Kashem, R. Döhrmann, R. Gehrke, A. Rothkirch, K. Stassig, W. Wurth, G. Benecke, C. Li, P. Fratzl, M. Rawolle, P. Müller-Buschbaum, *J. Phys. Condens. Matter* **2011**, *23*, 254208.
- [74] S. V. Roth, T. Autenrieth, G. Grübel, C. Riekel, M. Burghammer, R. Hengstler, L. Schulz, P. Müller-Buschbaum, *Appl. Phys. Lett.* **2007**, *91*, 91915.
- [75] T. Kassar, M. Berlinghof, N. S. Güldal, T. Schmutzler, F. Zontone, M. Brandl, E. Metwalli, J. Will, N. Li, T. Ameri, C. J. Brabec, T. Unruh, *Sol. RRL* **2019**.
- [76] A. Buffet, A. Rothkirch, R. Döhrmann, V. Körstgens, M. M. Abul Kashem, J. Perlich, G. Herzog, M. Schwartzkopf, R. Gehrke, P. Müller-Buschbaum, S. V. Roth, *J. Synchrotron Rad.* **2012**, *19*, 647.
- [77] G. Benecke, W. Wagermaier, C. Li, M. Schwartzkopf, G. Flucke, R. Hoerth, I. Zizak, M. Burghammer, E. Metwalli, P. Müller-Buschbaum, M. Trebbin, S. Förster, O. Paris, S. V. Roth, P. Fratzl, *J. Appl. Crystallogr.* **2014**, *47*, 1797.